Konrad-Zuse-Zentrum
für Informationstechnik Berlin

Takustraße 7
D-14195 Berlin-Dahlem
Germany

MARTIN WEISER MATHIAS RÖLLIG
RALF ARNDT BODO ERDMANN

Development and test of a numerical model for pulse thermography in civil engineering

ZIB-Report 08-45 (December 2008)

Development and test of a numerical model for pulse thermography in civil engineering

Martin Weiser* Mathias Röllig‡ Ralf Arndt§ Bodo Erdmann¶

January 7, 2009

Abstract

Pulse thermography of concrete structures is used in civil engineering for detecting voids, honeycombing and delamination. The physical situation is readily modeled by Fourier's law. Despite the simplicity of the PDE structure, quantitatively realistic numerical 3D simulation faces two major obstacles. First, the short heating pulse induces a thin boundary layer at the heated surface which encapsulates all information and therefore has to be resolved faithfully. Even with adaptive mesh refinement techniques, obtaining useful accuracies requires an unsatisfactorily fine discretization. Second, bulk material parameters and boundary conditions are barely known exactly. We address both issues by a semi-analytic reformulation of the heat transport problem and by parameter identification. Numerical results are compared with measurements of test specimens.

AMS MSC 2000: 80M10, 65M50
PACS 2008: 44.05.+e, 44.20.+b

Keywords: finite element model, KARDOS, pulse thermography, civil engineering, inverse solution

1 Introduction

Pulse thermography is a non-destructive testing method, which is widely used for the qualitative and quantitative defect detection in various structures. In pulse thermography the cooling process of a component is measured with an infrared camera

*Zuse Institute Berlin, Takustr. 7, 14195 Berlin, Germany (weiser@zib.de)
‡Bundesanstalt für Materialforschung und -prüfung, Unter den Eichen 87, 12205 Berlin, Germany (mathias.roellig@bam.de)
§FHWA NDE Center, Turner-Fairbank Highway Research Center, 6300 Georgetown Pike, McLean, VA 22101, USA (ralf.arndt@fhwa.dot.gov)
¶Zuse Institute Berlin, Takustr. 7, 14195 Berlin, Germany (erdmann@zib.de)

after heating (compare Fig. 1a and b), so that for every point on the component's surface a transient of the temperature is recorded. The transients differ for areas with inhomogeneities close to the surface if these have other thermal properties than the surroundings (compare Fig. 2b). Therefore the evaluation of the transients allows a qualitative detection of defects.

Quantitative results are available either in analytical form for ideal situations with short pulse heating and homogeneous materials, or alternatively by numerical simulation. However, with available numerical algorithms, inhomogeneous building materials, and long heating times required in civil engineering, the results turned out to be rather inaccurate.

2 State of the Art

Direct comparisons of experimental data and numerical simulations performed in the past for applications in civil engineering have shown that the predictive character of simulation is more of a qualitative than a quantitative nature [12]. There are simple analytical models for 1D and 2D problems available, which provide rough estimates of the temperature distribution [1]. Modeling based on finite differences was applied to 3D heat transfer with cylindrical coordinates [9]. Nowadays, the finite element methods with correct treatment of the experimental conditions is reported to be the most promising tool for modeling the heat transfer in 3D [4, 10, 2, 11]. Several commercial software packages are available with integrated CAD systems. However, due to the highly multiscale complexity of the problem, reliable quantitative results can only be obtained at very high computational cost.

The main contribution of the current paper is a method that combines analytical solutions for idealized situations with numerical compuation of the difference between actual and idealized situation. This allows to compute accurate simulations at moderate cost.

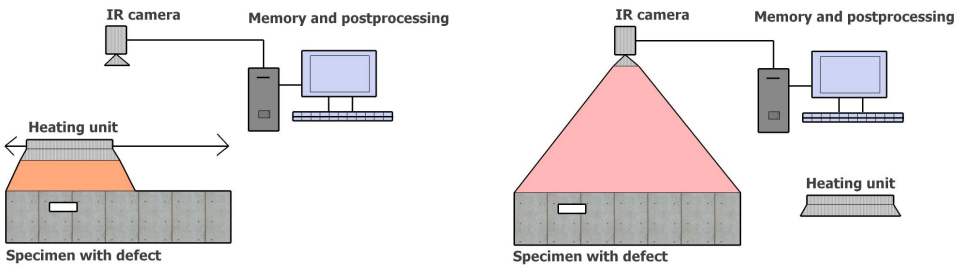

Figure 1: Principle of the heating (a) and measuring (b) of a test specimen with pulse thermography

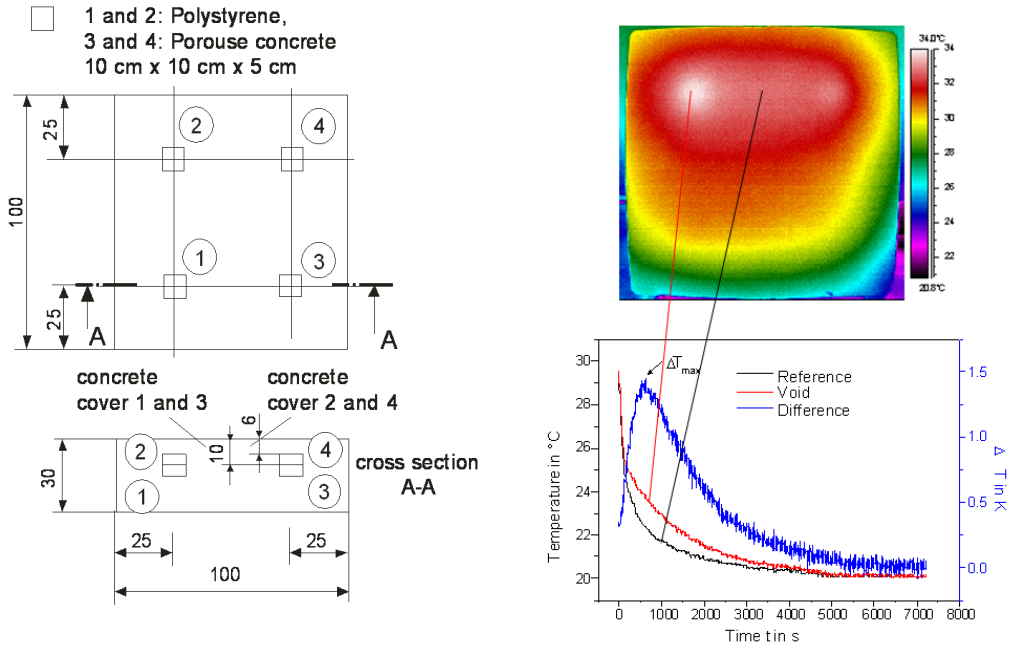

(a) (b)

Figure 2: Sketch of a test body (a), temperature profile after heating and recorded temperature transients (b)

3 Mathematical model

We assume the heated surface is planar and covers a domain $\Omega_0 \subset \mathbb{R}^2$. Extending Ω_0 into $\mathbb{R}^3$, the concrete material is assumed to occupy a prismatic domain $\Omega = \Omega_0 \times [0, z]$, where $z > 0$ is the thickness of the material. Now the temperature evolution is given by

$$\rho c \dot{T} = \operatorname{div}(\kappa \nabla T) \qquad \text{in } \Omega \tag{1}$$

$$\kappa \partial_n T = Q + g(T) \qquad \text{on } \partial\Omega \tag{2}$$

$$T = T_0 \qquad \text{for } t = 0 \tag{3}$$

For a description of the quantities we refer to Table 1.

According to the thermography setting with a time interval $[0, t_h]$ of constant heating, we assume that $Q(x,t) = Q_0(x_{1,2})\chi_{[0,t_h]}(t)\delta_{x_3}$. The Kronecker-$\delta$ factor restricts the heating to the front face of Ω while the characteristic function χ restricts the heat flux to the heating time interval. $Q_0 : \Omega_0 \to \mathbb{R}$ describes the spatial power density on the front face. The remaining heat flux across the boundary is a combination

Quantity	Symbol	Unit
time	t	s
position	x	m
temperature	T	K
thermal conductivity	κ	$W/(mK)$
density	ρ	kg/m^3
specific heat capacity	c	$J/(kgK)$
boundary heat flux	g	W/m^2
transversal convective heat transfer coefficient	h_{trans}	$W/(m^2K)$
radiation coefficient	C_{trans}	$W/(m^2K^4)$
heating	Q_0	W/m^2

Table 1: Physical quantities appearing in the mathematical model of pulse thermography.

of convective and radiative heat transfer:

$$g(T) = g(T; h_{\text{trans}}, T_{\text{ext}}, C_{\text{trans}}, T_{\text{amb}}) = h_{\text{trans}}(T_{\text{ext}} - T) + C_{\text{trans}}(T_{\text{amb}}^4 - T^4)$$

4 Treatment of boundary layers

If thermal diffusivity $\kappa/(\rho c)$ and heating time t_h are very small compared to the front surface area $|\Omega_0|$, the solution T exhibits a very thin boundary layer, which is the case for realistic material, geometries, and heating times. This boundary layer has to be represented accurately in numerical computation, since it essentially determines the solution. Too coarse a discretization leads to a too fast transport of simulated heat from the boundary layer into the interior of the material.

The mesh width that is necessary in the boundary layer in order to obtain reasonable accuracies can lead to problem sizes that are beyond reasonable computing facilities. For example, discretizing the setup of Section 7.1 with trilinear elements on uniform isotropic meshes and aiming at an absolute averaged temperature error of $10^{-2}K$ would require about 600 million degrees of freedom and a roughly estimated computing time of around 1000 hours on a current PC. More sophisticated meshing strategies, e.g., self-adaptive meshes or mesh grading towards the heated surface can reduce the computational complexity tremendously, but still do not obtain reasonable accuracies in real time.

The choice of an efficient meshing is complicated by the fact that as the temperature distribution evolves, it becomes increasingly smooth, and the boundary layer vanishes. Repeated mesh adaptation or changes in the mesh grading, respectively, is necessary to provide efficient discretizations as the simulated time proceeds.

4.1 Semi-analytic approximation

A different approach that we pursue here is to capture the boundary layer with an analytically obtained approximation, and computing only the remaining defect numerically. The semi-analytical approximation is derived for a simplified situation with homogeneous material, linear and translation-invariant boundary conditions, and a half-space as domain. In this setting, the temperature increase u_0 due to heating satisfies a linear 1D PDE that can be addressed by analytical means and is moreover linear in the heating intensity Q_0, such that it can easily be scaled by a given power distribution on the heating surface.

The simplified 1D model is given as

$$\rho_0 c_0 \dot{u}_0 = \kappa_0 u_0'' \qquad \text{in } \mathbb{R}_+ \tag{4}$$

$$-\kappa_0 u_0' = \chi_{[0,t_h]} + \bar{g}'(\bar{T}) u_0 \qquad \text{on } \partial\mathbb{R}_+ \tag{5}$$

$$u_0(x,0) = 0. \tag{6}$$

Since u_0 is intended to capture the boundary layer at the front surface, the homogeneous material parameters ρ_0 and κ_0 are chosen as averages of those on the front surface. In order to approximate the boundary conditions well, we average the coefficients h_{trans}, T_{ext}, C_{trans}, and T_{amb} over Ω_0, which yields the averaged heat flux $\bar{g}(T) = g(T; \bar{h}_{\text{trans}}, \bar{T}_{\text{ext}}, \bar{C}_{\text{trans}}, \bar{T}_{\text{amb}})$. This is linearized around a temperature $\bar{T}$ that should be roughly the midpoint of the range covered by the front surface temperature distribution.

We extend u_0 to an approximate 3D solution u by multiplying with the heating power distribution:

$$u(x) = Q_0(x_{1,2}) u_0(x_3) \tag{7}$$

Note that due to this construction we have

$$\nabla u(x,t) = \begin{bmatrix} u_0(x_3,t) \nabla Q_0(x_{1,2},t) \\ Q_0(x_{1,2},t) u_0'(x_3,t) \end{bmatrix}. \tag{8}$$

Now we set $T = u + \delta u$, such that (1) and (3) read

$$\begin{aligned} \rho c(\dot{u} + \dot{\delta u}) &= \operatorname{div}(\kappa \nabla u) + \operatorname{div}(\kappa \nabla \delta u) \\ &= u_0 \operatorname{div}(\kappa \nabla Q_0) + \partial_3(Q_0 \kappa u_0') + \operatorname{div}(\kappa \nabla \delta u) \\ &= u_0 \operatorname{div}(\kappa \nabla Q_0) + Q_0 \kappa_0 u_0'' + Q_0 \partial_3((\kappa - \kappa_0) u_0') + \operatorname{div}(\kappa \nabla \delta u) \\ \delta u &= T_0 \quad \text{for } t = 0 \end{aligned}$$

Moving the time derivative of u to the right hand side and using (8) and (4), we have

$$\begin{aligned} \rho c \dot{\delta u} &= u_0 \operatorname{div}(\kappa \nabla Q_0) + Q_0 \partial_3((\kappa - \kappa_0) u_0') + \operatorname{div}(\kappa \nabla \delta u) - (\rho c - \rho_0 c_0) \dot{u} \\ &\quad + Q_0 \kappa_0 u_0'' - Q_0 \rho_0 \dot{u}_0 \\ &= u_0 \operatorname{div}(\kappa \nabla Q_0) + Q_0 \partial_3((\kappa - \kappa_0) u_0') + \operatorname{div}(\kappa \nabla \delta u) - (\rho c - \rho_0 c_0) \dot{u}. \end{aligned} \tag{9}$$

We see that δu satisfies the same PDE as T, except for the additional source term

$$f = u_0 \mathrm{div}(\kappa \nabla Q_0) + Q_0 \partial_3((\kappa - \kappa_0)u_0') - (\rho c - \rho_0 c_0)\dot{u}. \tag{10}$$

Using (5), we see that on the front face, the boundary condition (2) is

$$\begin{aligned} \kappa \partial_n \delta u &= Q + g(T) - \kappa \partial_n u \\ &= Q + g(T) + \kappa Q_0 u_0' \\ &= Q_0 \chi_{[0,t_h]} + g(T) - Q_0 \left(\chi_{[0,t_h]} + \bar{g}'(\bar{T})u_0\right) \\ &= g(Q_0 u_0 + \delta u) - \bar{g}'(\bar{T}) Q_0 u_0. \end{aligned} \tag{11}$$

Note that in particular the external heating Q is completely eliminated from the boundary condition for δu, and that the first two moments of the boundary condition associated to u are small if the spatial variation of the boundary data is small. On the back face of the boundary, (2) translates to

$$\kappa \partial_n \delta u = g(Q_0 u_0 + \delta u) - \kappa Q_0 u_0',$$

whereas on the side faces it reduces to

$$\kappa \partial_n \delta u = g(Q_0 u_0 + \delta u) - \kappa u_0 \partial_n Q_0. \tag{12}$$

4.2 Evaluation of the analytical approximation

For the actual computation of δu with a finite element method we need to evaluate u_0, u_0', and $\dot{u}_0$, and thus have only shifted the problem of representing the boundary layer from 3D to 1D. In the following we will work out how to compute u_0 and its derivatives.

Using the fundamental solution

$$G(x,t) = \frac{\sqrt{\rho_0 c_0}\exp(-\frac{\rho_0 c_0 x^2}{4\kappa_0 t})}{\sqrt{4\pi\kappa_0 t}}, \quad t > 0,$$

for the heat transfer equation, u_0 is given by

$$u_0(x,t) = \int_{\tau=0}^{t} \frac{2}{\rho_0 c_0} \left(\chi_{[0,t_h]}(\tau) + \bar{g}'(\bar{T})u_0(0,\tau)\right) G(x, t-\tau)\, d\tau, \tag{13}$$

see [6, Chap. 2.3]. Unfortunately, no closed analytical expression for (13) seems to exist. Once again we may approximate u_0 by an analytical expression and compute the defect numerically. To this extend we substitute a rational expression for the exponential and rewrite (13) as

$$\begin{aligned} \frac{\rho_0 c_0}{2} u_0(x,t) = \int_{\tau=0}^{\min(t,t_h)} \hat{G}(x,t-\tau)\, d\tau + \int_{\tau=0}^{\min(t,t_h)} (G(x,t-\tau) - \hat{G}(x,t-\tau))\, d\tau \\ + \int_{\tau=0}^{t} \bar{g}'(\bar{T}) u_0(0,\tau) G(x,t-\tau)\, d\tau \end{aligned} \tag{14}$$

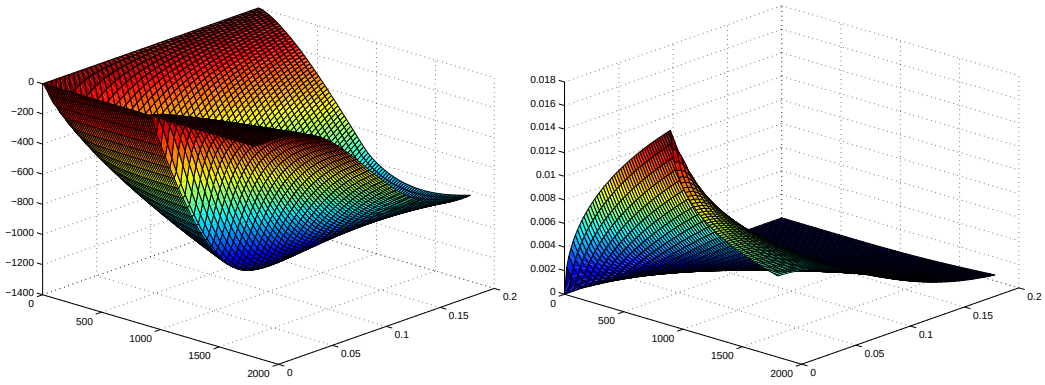

Figure 3: Numerically computed correction δH (left) idealized solution u_0 (right) on the domain $x \in [0, 0.2]m$, $t \in [0, 1800]s$ for the material paramters given in Table 6 and boundary conditions in Table 2 with $\bar{T} = 290K$.

with

$$\hat{G}(x,t) = \sqrt{\frac{\rho_0 c_0}{4\pi\kappa_0 t}} \left(1 + \frac{\rho_0 c_0 x^2}{4\kappa_0 t}\right)^{-1}.$$

Now the first integral in (14) is given analytically as

$$H(x,t) = \frac{\rho_0 c_0 x}{2\kappa_0\sqrt{\pi}} \left(w\left(\sigma\sqrt{t}\right) - w\left(\sigma\sqrt{t - \min(t, t_h)}\right)\right)$$

with

$$\sigma = \frac{2}{x}\sqrt{\frac{\kappa_0}{\rho_0 c_0}} \quad \text{and} \quad w(\tau) = \tau - \arctan\tau. \tag{15}$$

Note that for $\tau \to 0$ the evaluation of $w(\tau)$ according to (15) is unstable and, using double accuracy arithmetics, should be replaced by the Taylor series approximation $w(\tau) \approx \tau^3/3$ for $\tau < 10^{-4}$.

Next we define

$$\delta H(x,t) = \int_{\tau=0}^{\min(t,t_h)} (G(x, t-\tau) - \hat{G}(x, t-\tau))\, d\tau + \int_{\tau=0}^{t} \bar{g}'(\bar{T}) \frac{2}{\rho_0 c_0} (H(0,\tau) + \delta H(0,\tau)) G(x, t-\tau)\, d\tau, \tag{16}$$

which needs to be treated numerically. Since δH is defined over a rectangular area in $\mathbb{R}^2$, it is easily possible to numerically integrate and store δH and its derivatives on a sufficiently fine cartesian grid. For $x = 0$, (16) is a Volterra equation of second kind. For integration methods, in particular for handling the singular kernel $G(0, \cdot)$ in the Volterra equation, we refer to [6].

5 Initial and boundary conditions

Efficient and accurate solution of the heat equation (1) - (3) is necessary, but not sufficient to obtain quantitatively correct temperature distributions. Of vital importance for the agreement of simulation and measurements is the estimation of boundary conditions and the initial state T_0 of the temperature distribution. Neither 3D temperature measurements of the specimen nor exact data about external temperature T_{ext} and ambient radiation temperature T_{amb} are commonly available.

We assume that the specimen is in thermal equilibrium. For lack of better data, we extend the front face temperature measurement normal to the front face, giving a guess T_0^m of the complete boundary temperature. In principle, we could solve the Dirichlet problem for T_0 and compute T_{ext} from

$$T_{\text{ext}} = T_0^m + h_{\text{trans}}^{-1} \left(\kappa \partial_n T_0 - C_{\text{trans}} (T_{\text{amb}}^4 - T_0^4) \right). \tag{17}$$

However, noise in T_0^m would be significantly amplified by this approach. Instead we start with (17), where we compute $\partial_n T_0$ from the very coarse but smooth model

$$T_0(x) \approx T_{\text{bottom}} + \frac{x_2}{H} (T_{\text{top}} - T_{\text{bottom}})$$

to account for the vertical temperature gradient in x_2-direction that is clearly visible in the initial measurements. T_{top} and T_{bottom} are the averaged top and bottom face temperatures, respectively, and H is the height of the specimen. With T_{ext} given by (17), we solve

$$\begin{aligned} \operatorname{div}(\kappa \nabla T_0) &= 0 && \text{in } \Omega \\ \kappa \partial_n T_0 &= h_{\text{trans}} (T_{\text{ext}} - T_0) + C_{\text{trans}} (T_{\text{amb}}^4 - T_0^4) && \text{on } \partial\Omega \end{aligned}$$

for the stationary initial value T_0 shown in Fig. 4.

6 Characterization of the IR heating unit

Since the nonuniformity of the heating is quite important [10], in this section we derive an expression for the power distribution Q_0 imposed by the IR heating unit on the front surface.

First we consider the power distribution caused by an isotropic point source of distance d to the front face. Assume the power emitted per steradian is P_0. The power contained in a narrow square pyramid with opening angle γ is then $\gamma^2 P_0$. Assume the center line of the pyramid forms an angle α with the normal of the front face. The intersection of the pyramid with the front face has an area

$$A = \frac{\gamma^2 d^2}{(\cos \alpha)^3}$$

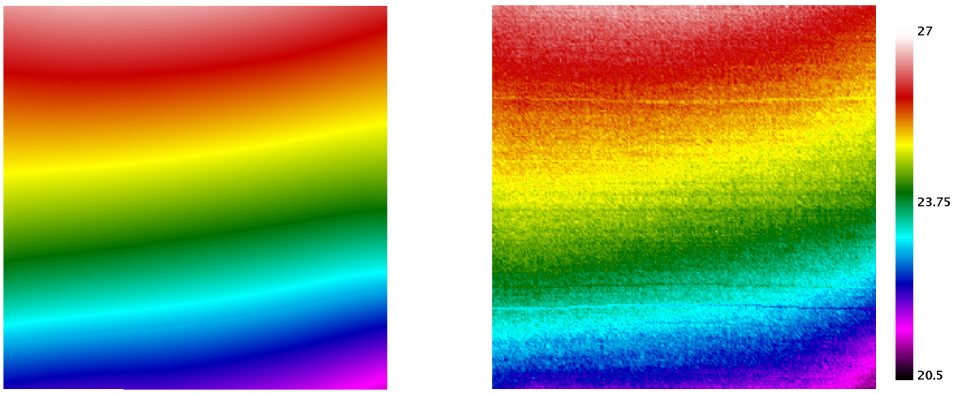

(a) simulation at t=0 (b) measurement at t=0

Figure 4: Initial temperature distribution T_0 on the front face (a) and noisy measurement (b) just before heating

over which the power $\gamma^2 P_0$ is distributed. Thus, the power density on the front face is given by

$$P(x) = \frac{P_0(\cos\alpha)^3}{d^2} = \frac{P_0 d}{l(x,s)^3},$$

where $l(s,x)$ is the distance between the source point s and a point x on the front face.

The heating unit consists of several vertical cylindrical emitters heated to approximately $900K$. The front surface of the specimen is heated approximately uniformly by a periodic horizontal movement of the heating unit. Compared to the temperature dynamics, the horizontal movement has a high frequency, such that the periodic temperature variation is quickly averaged out [7]. For this reason, we model the heating unit as a superposition of rectangular area sources, one for each heated rod. The points on the area sources are assumed to emit an isotropic radiation. Then the power density induced by an area source covering the area R is given by

$$P(x) = P_0 d \int_R l(s,x)^{-3}\, ds$$

and for the whole heating unit with several heated emitters the power density is simply the sum

$$P(x) = P_0 d \sum_i \int_{R_i} l(s,x)^{-3}\, ds.$$

The heating unit used in Section 7.1 consists of two vertically aligned groups of Heraeus MMS 2400 infrared modules. Each module contains three parallel vertical emitters with a horizontal distance of $6.7cm$. The vertical distance between the

modules is close to zero. The length of the emitters is 50 cm but we have to consider that the emitters are not effective within $3cm$ of their ends. The horizontal movement of the heating unit covers $1.04m$. The back face of the emitters is covered by a reflective coating, such that only a small amount of energy, approximately 9%, is emitted backwards. Behind the emitters an aluminum sheet in 3 cm distance reflects about 70% of this fraction to the front. The effect of the reflective aluminum sheet is modeled as a second array of heating emitters in a distance of 6 cm behind the primary emitters, with a relative power of 7%. The power distribution generated on the front face of the specimen is shown in Fig. 5.

7 Numerical simulations of active thermography

In this section we compare the simulation result with measurements for a concrete test specimen. The FE simulations have been performed with the adaptive finite element code KARDOS [5].

7.1 Experimental setup

A concrete test specimen with defined defects was constructed having a size of $1 \times 1 \times 0.3m^3$ and containing two polystyrene and two porous concrete cuboids

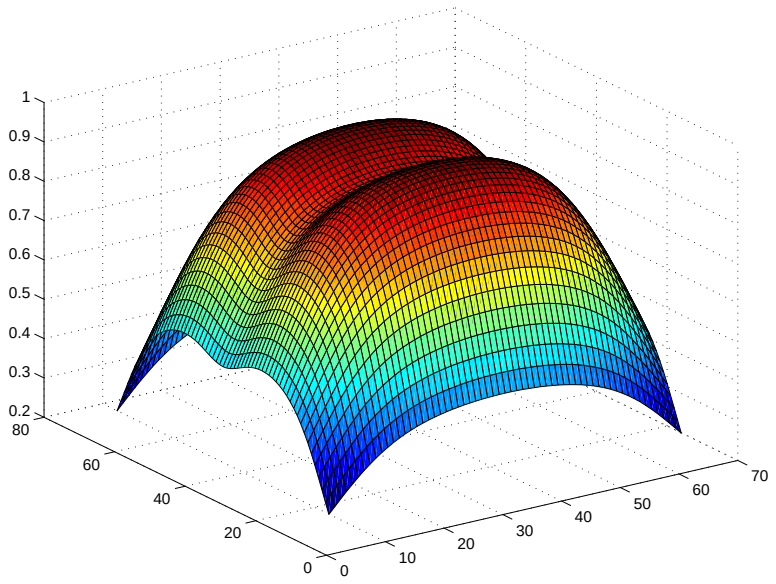

Figure 5: Power distribution Q_0 on the specimen's surface as induced by the IR heating unit used in Section 7.1. The central groove is caused by the gap between the emitters.

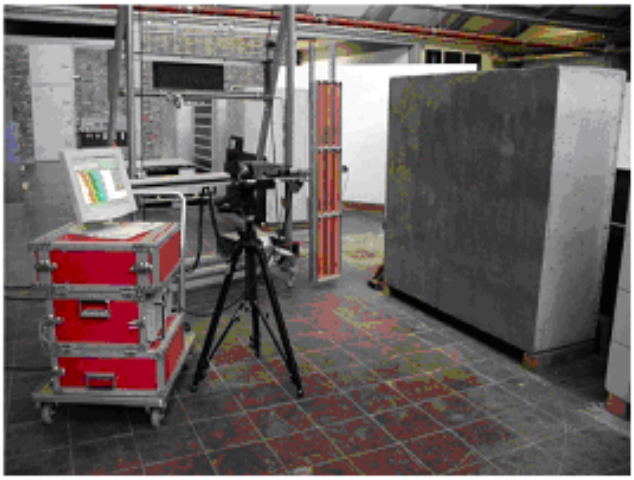

Figure 6: Laboratory set-up with IR heating unit, IR camera and investigated specimen.

with a size of $10 \times 10 \times 5cm^3$ with concrete covers of $6cm$ and $10cm$ (see Fig. 2, left). A grain size distribution curve of A/B 16 and a water/cement ratio of 0.6 were realized for the concrete mixture. The air content in fresh concrete was about (0.9 ± 0.2) Vol%. The compressive strength and density determined at 28 days old cubes were $(48.5 \pm 2.0)N/mm^2$ and $(2.33 \pm 0.03)kg/dm^3$, respectively. The investigations presented in the following were performed one year after concreting. The experimental set-up for the performed measurements with pulse thermography is shown in Fig. 6. It consists of a thermal heating unit (one to three IR-radiators with $2400W$ power each) which are moved periodically in front of the investigated specimen, a commercial infrared camera (Inframetrics SC1000, 256x256 pixels in a wavelength range of $3 - 5\mu m$) and a computer system, which enables digital data recording in real time. The heating time was $t_h = 900s$ and the observation time was $t_{\text{obs}} = 7200s$ with a measured frame rate of $2Hz$, averaged to computed $0.2Hz$. With T_m we denote the temperature measurements.

Quantity	**Value**	
Heat transfer coefficient h_{trans}	6.2800e+00	$W/(m^2K)$
Radiation constant C_{trans}	5.6705e-08	$W/(m^2K^4)$
Power Q_0 (spatially constant)	1.7000e+03	W/m^2
Ambient temperature T_{amb}	2.9300e+02	K

Table 2: Specified boundary conditions

7.2 Numerical simulation

Numerical simulations of the pulse thermography of concrete-test specimen PKII1 (see drawing in Fig. 2a) were carried out with both the straightforward purely numerical and the presented semi-analytic method. The boundary conditions used are given in Table 2, the material properties in Table 3. Two different coarse grids have been used with each method, an isotropic mesh and a graded mesh with rather flat tetrahedra at the front surface.

Error control is realized by adaptive mesh refinement until the estimated averaged absolute error in each time step falls below a specified bound TOL. Resulting refined meshes are shown in Fig. 7. As expected, the purely numerical method needs to refine the mesh at the whole front face of the specimen in order to represent the boundary layer. In the semi-analytic approach, the boundary layer is captured by the idealized analytic solution, such that the FE solution needs to represent only the actual deviation δu. This is largest where the idealized situation is violated by the actual setup. These are the edges, where the translation invariance is violated, and the interior defect cuboids, where the assumption of homogeneous material is violated. Consequently, in Fig. 7 moderate refinement is visible at the edges of the specimen.

Required degrees of freedom, computing time on a $2.6GHz$ Opteron processor, and obtained maximal temperature after $100s$ of heating are reported for different tolerances in Tables 4 and 5. A gain of factor 20 both in degrees of freedom and computing time is observed for the purely numerical method when switching from an isotropic to an anisotropic coarse grid. The semi-analytic method achieves a remarkable performance gain of factor 500–1000. For the semi-analytic method both coarse meshes work comparatively well, the isotropic mesh even somewhat better. This is to be expected since the deviation δu does not contain an anisotropic boundary layer, such that the additional mesh vertices incurred by the anisotropic grading

Material	**Quantity**	**Value**	
Concrete	Density ρ	2,400.00	kg/m^3
	Specific heat capacity c	1,000.00	J/kgK
	Heat conductivity κ	2.10	W/mK
Polystyrene	Density ρ	500.00	kg/m^3
	Specific heat capacity c	1,000.00	J/kgK
	Heat conductivity κ	0.04	W/mK
Gas concrete	Density ρ	500.00	kg/m^3
	Specific heat capacity c	1,000.00	J/kgK
	Heat conductivity κ	0.16	W/mK

Table 3: Material properties according to DIN 4108

just increase the number of degrees of freedom without providing any accuracy improvement.

Two more points need to be noted. First, with simulated time progressing, the boundary layer in the solution is smoothed out and vanishes eventually, such that the efficiency gain decreases over time. Second, as can be seen from the $T_{\max}$ values in Tables 4 and 5, the local error bound TOL does not correspond exactly to the global error. In particular the global error appears to be much smaller for the semi-analytical method than it is for the purely numerical method with same tolerance.

7.3 Parameter identification

The depth of a defect correlates strongly with the time at which the surface temperature difference between a point above the defect and a point above bulk material

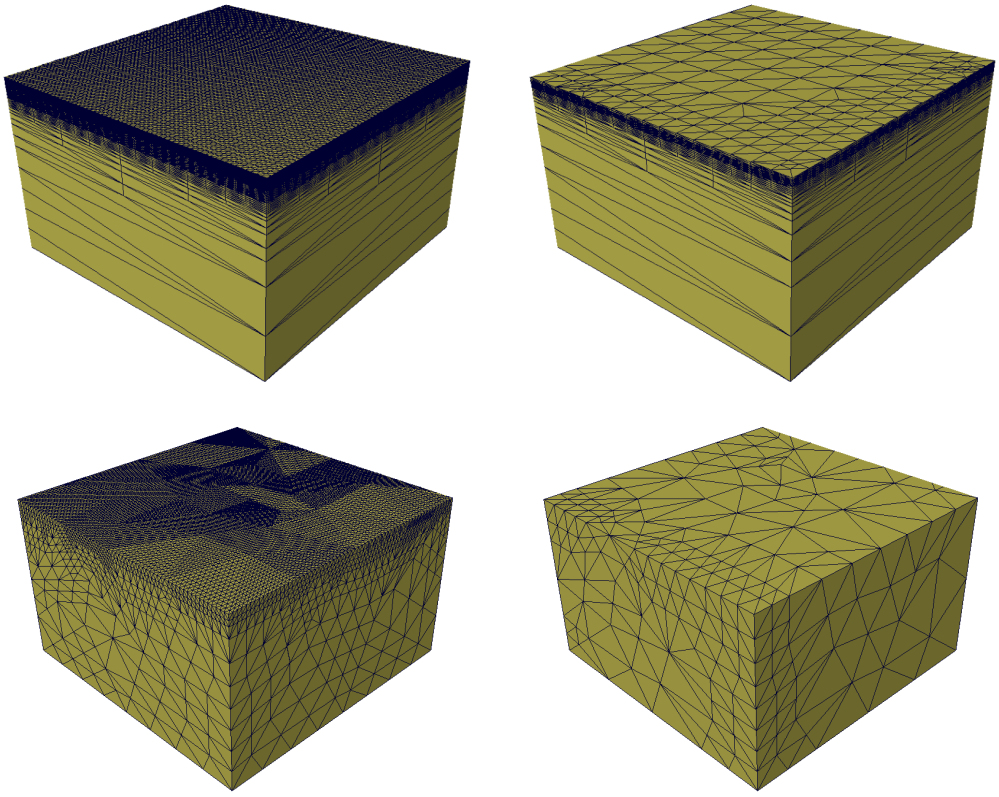

Figure 7: Adaptively refined anisotropic (top) and isotropic (bottom) coarse mesh at $t = 100s$ by purely numerical (left) and semi-analytical (right) method producing the same accuracy in the solution.

	semi-analytical			purely numerical		
TOL	$\mathbf{T}_{\max}$ [K]	**N**	**CPU** [s]	$\mathbf{T}_{\max}$ [K]	**N**	**CPU** [s]
1e-2	306.894	445	2	307.199	224,140	702
5e-3	306.895	1,045	3	307.290	511,539	2,370
2e-3	306.921	2,337	11	307.324	2,415,306	11,230
1e-3	306.919	9,567	28	307.138	5,115,356	54,358
5e-4	306.921	18,869	67			
2e-4	306.921	69,447	538			
1e-4	306.921	239,911	2,372			

Table 4: Semi-analytical and purely numerical computation for different tolerances, starting on isotropic coarse mesh. Both methods use adaptive mesh refinement to satisfy the accuracy requirement. Maximal temperature $T_{\max}$ on the surface, the number N of degrees of freedom, and the computing time are reported.

	semi-analytical			purely numerical		
TOL	$\mathbf{T}_{\max}$ [K]	**N**	**CPU** [s]	$\mathbf{T}_{\max}$ [K]	**N**	**CPU** [s]
1e-2	306.920	6,917	15	307.009	9,817	24
5e-3	306.921	6,881	24	307.060	19,901	72
2e-3	306.920	9,824	48	307.150	100,644	382
1e-3	306.920	13,433	63	307.217	237,592	1,440
5e-4	306.921	17,723	143	307.177	602,206	6,641
2e-4	306.919	107,775	681	307.145	3,060,661	37,561
1e-4	306.919	317,654	3,730			

Table 5: Semi-analytical and purely numerical computation for different tolerances, starting on anisotropic mesh graded towards the front face. Both methods use adaptive mesh refinement to satisfy the accuracy requirement. Maximal temperature $T_{\max}$ on the surface, the number N of degrees of freedom, and the computing time are reported.

is maximal [12, 7, 8]. Therefore a correct time of simulated surface temperature differences is of interest. Fig. 8 shows the temperature difference between a point above the top left defect and the center of the front face. The comparison shows that the simulated temperature difference curve (Simulation I) exhibits a significant delay compared to the measured one. Since the simulation results with error control are sufficiently accurate, it can be assumed that the used model parameters of Tables 2 and 3 do not correspond to the reality.

In order to improve the agreement between simulation and measurement, the geometrically derived power distriubtion from Section 6 has been developed and a preliminary identification was conducted for a set of relevant parameters. These were the irradiation power P_0, heat capacity c and conductivity κ of the concrete. A square grid of nine points x_i on the front face of the specimen was selected for

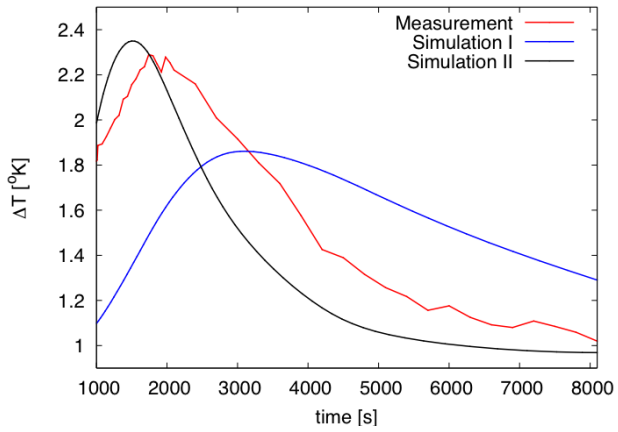

Figure 8: Temperature difference between two front surface points above a defect and above bulk material. Measured data and simulations for different material parameters.

Quantity	**Identified value**	**Given value**	**Deviation**
c_{concrete}	5.0411e+02	1.0000e+03	49.6%
κ_{concrete}	3.4290e+00	2.1000e+00	-63.3%
P_0	1.34634e+03	1.7000e+03	20.8%

Table 6: Identified parameters and boundary conditions

formulating the following least squares problem:

$$\min \sum_{i=1}^{9} \|T(x_i) - T_m(x_i)\|^2_{L^2([t_h, t_h+t_{\text{obs}}])}$$

A damped Gauß-Newton method (cf. [3]) has been used for the solution. The required gradients were gained by internal numerical differentiation.

A clear reduction about factor three of the mismatch has been achieved by identification of the three selected parameters. This simulation (Simulation II) also led to a clear reduction of the time offset in the temperature difference curves (see Fig. 8).

The identified parameters in Table 6 partly deviate significantly from the given values, but are still in a physically sensible range. Nonetheless these values have to be interpreted with care since no inhomogeneities are considered besides the given defects and many model parameters are not adapted at all.

The results of the simulations carried out with the proposed analytic-numerical hybrid method show a good correspondence with the measured values, see Fig. 9. The observed differences at the investigated times are below $1K$. Due to careful estimation of the initial temperature distribution, geometrical modeling of the heat

source, and identification of relevant material parameters, the simulated temperature evolution agrees very well with the measured one.

Summary and conclusions

A hybrid analytic-numerical procedure has been developed which permits quantitatively reliable simulations of pulse thermography at moderate computational cost. The identification carried out for three relevant parameters and a measuring film led to a significant reduction of the time error in the temperature difference curve maxima. In particular the careful treatment of initial and boundary conditions has a large influence. The achieved simulation results are clearly better than comparable results from literature [12, 7, 8]. Hence, increased reliability for quantitative prediction of data is possible, which is also a prerequisite for the development of methods for the quantitative identification of spatially distributed material parameters.

Acknowledgements. The authors would like to thank M. Zänker for contributing to Section 6 and C. Nowzohour for contributing to Section 4.

References

[1] J.C. Carslaw, H.S. und Jaeger. *Conduction of heat in solids.* Clarendon Press, 2 edition, 1959.

[2] P. Chaudhuri, P. Santra, S. Yoele, A. Prakash, D.C. Reddy, L.T. Lachhvani, J. Govindarajan, and Y.C. Saxena. Non-destructive evaluation of brazed joints between cooling tube and heat sink by IR thermography and its verification using FE analysis. *NDT&E International*, 39:88–95, 2006.

[3] P. Deuflhard. *Newton Methods for Nonlinear Problems. Affine Invariance and Adaptive Algorithms*, volume 35 of *Computational Mathematics.* Springer, 2004.

[4] M. Krishnapillaia, R. Jonesa, I.H. Marshalla, M. Bannisterb, and N. Rajicc. NDTE using pulse thermography: Numerical modeling of composite subsurface defects. *Composite Structures*, 75:241–249, 2006.

[5] J. Lang. *Adaptive Multilevel Solution of Nonlinear Parabolic PDE Systems*, volume 16 of *Lecture Notes in Computational Science and Engineering.* Springer, 2001.

[6] P. Linz. *Analytical and Numerical Methods for Volterra Equations.* Studies in Applied Mathematics. SIAM, 1985.

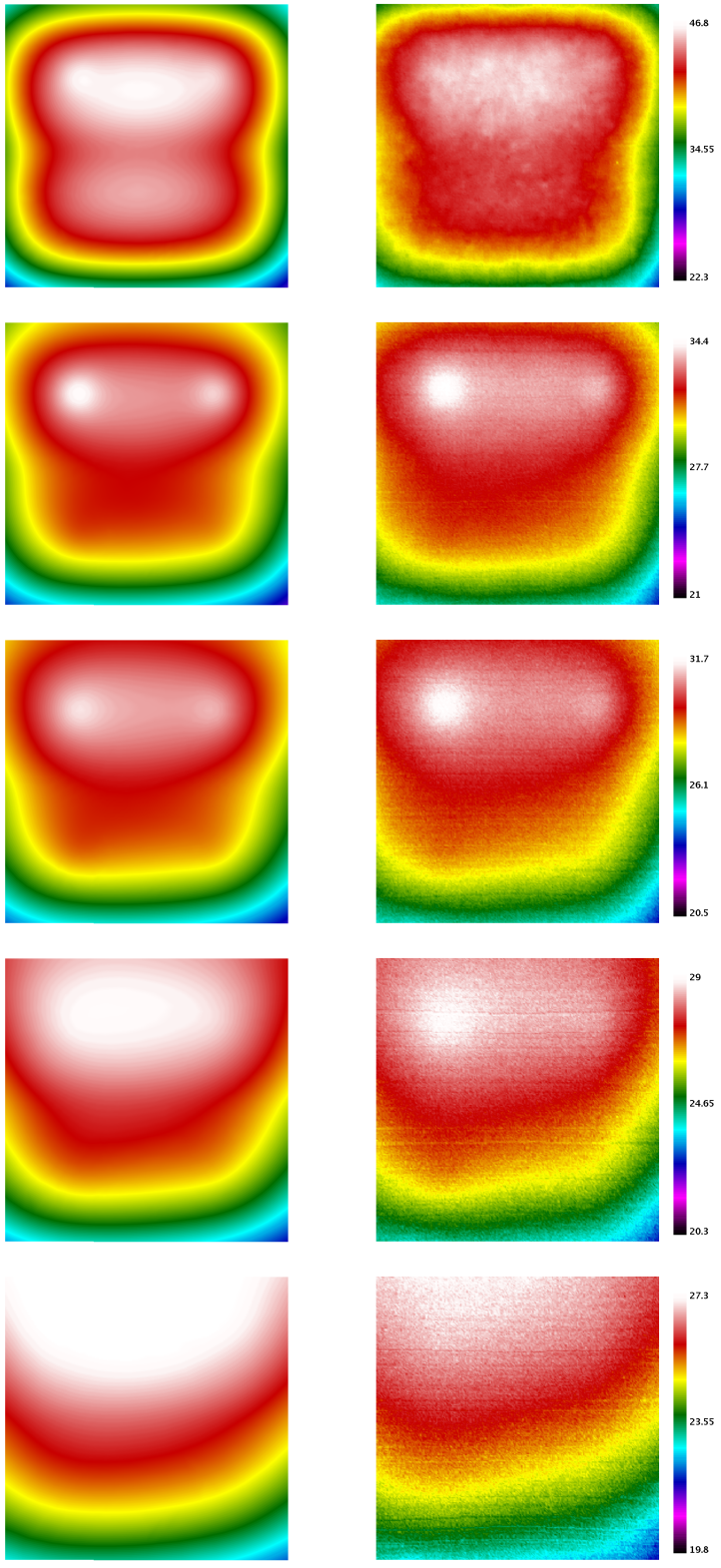

Figure 9: Simulation results (left) and corresponding measurements (right) at $10s$, $900s$, $1800s$, $3600s$, and $7200s$ after the end of heating. Note that the temperature range covered by the front face shrinks over time and hence the color coding changes.

[7] Ch. Maierhofer, R. Arndt, M. Röllig, A. Brink, H. Wiggenhauser, B. Hillemeier, C. Rieck, A. Walther, and H. Scheel. Abschlussbericht zum DFG-Projekt Struktur- und Feuchteuntersuchungen von Bauteil- und Bauwerksoberflächen mit der Impulsthermographie, Teil 1 und Teil 2. Technical report, BAM, 2005.

[8] Ch. Maierhofer, A. Brink, M. Röllig, and H. Wiggenhauser. Quantitative impulse-thermography as non-destructive testing method in civil engineering — experimental results and numerical simulations. *Construction and Building Materials*, 19(10):731–737, 2005. Non Destructive Testing: Selected papers from Structural Faults and Repair 2003.

[9] X. Maldague. *Theory and Practice of Infrared Technology for Nondestructive Testing*. Wiley, 2001.

[10] M. Susa, C. Ibarra-Castanedo, X. Maldague, S. Svaic, I. Boras, and A. Bendada. Pulse thermography applied on a complex structure sample: comparison and analysis of numerical and experimental results. In *IV Pan American Conference in END*, Buenos Aires, Argentina, October 22-26 2007.

[11] V.P. Vavilov and A.G. Klimov. Studying the phenomena related to the IR thermographic detection of buried landmines. In *VI International Conference on Quantitative Infrared Thermography*, Dubrovnik, Croatia, September 24–27 2002.

[12] G. Wedler, A. Brink, Ch. Maierhofer, M. Röllig, F. Weritz, and H. Wiggenhauser. Active infrared thermography in civil engineering — quantitative analysis by numerical simulation. In *International Symposium on Non-Destructive Testing in Civil Engineering*, Berlin, September 16–19 2003. NDT-CE.